

# Rapid Magnetic Resonance Quantification on the Brain: Optimization for Clinical Usage

J.B.M. Warntjes,<sup>1–3\*</sup> O. Dahlqvist Leinhard,<sup>1,4</sup> J. West,<sup>1,3,4</sup> and P. Lundberg<sup>1,4</sup>

**A method is presented for rapid simultaneous quantification of the longitudinal  $T_1$  relaxation, the transverse  $T_2$  relaxation, the proton density (PD), and the amplitude of the local radio frequency  $B_1$  field. All four parameters are measured in one single scan by means of a multislice, multiecho, and multidelay acquisition. It is based on a previously reported method, which was substantially improved for routine clinical usage. The improvements comprise of the use of a multislice spin-echo technique, a background phase correction, and a spin system simulation to compensate for the slice-selective RF pulse profile effects. The aim of the optimization was to achieve the optimal result for the quantification of magnetic resonance parameters within a clinically acceptable time. One benchmark was high-resolution coverage of the brain within 5 min. In this scan time the measured intersubject standard deviation (SD) in a group of volunteers was 2% to 8%, depending on the tissue (voxel size =  $0.8 \times 0.8 \times 5$  mm). As an example, the method was applied to a patient with multiple sclerosis in whom the diseased tissue could clearly be distinguished from healthy reference values. Additionally it was shown that, using the approach of synthetic MRI, both accurate conventional contrast images as well as quantification maps can be generated based on the same scan. *Magn Reson Med* 60:320–329, 2008. © 2008 Wiley-Liss, Inc.**

**Key words:** quantitative MRI;  $T_1$  mapping;  $T_2$  mapping; PD mapping;  $B_1$  mapping; synthetic MRI; neurodegenerative disease

Tissues in the human body can be distinguished with magnetic resonance imaging (MRI) depending on their MR parameters, such as the longitudinal  $T_1$  relaxation, the transverse  $T_2$  relaxation, and the proton density (PD). In clinical routine, the MR scanner settings, such as echo time ( $T_E$ ), repetition time ( $T_R$ ), and flip angle ( $\alpha$ ), are most often chosen to highlight, or saturate, the image intensity of tissues, resulting in  $T_1$ -weighting or  $T_2$ -weighting in a contrast image. These procedures are well-established and relatively quick. A major disadvantage of using such contrast images is that the absolute intensity has no direct meaning and diagnosis relies on comparison with surrounding tissues in the image. In many cases it is therefore

necessary to perform several different contrast scans. A more direct approach is the absolute quantification of the tissue parameters  $T_1$ ,  $T_2$ , and PD. In this case, pathology can be examined on a pixel basis to establish the absolute deviation compared to the normal values. Automatic segmentation of such tissue images would be straightforward and the progress of the disease could then be expressed in absolute numbers. An excellent overview of the use of absolute quantification on neurodegenerative diseases is provided in Ref. 1.

Although the advantages of absolute quantification are obvious, its clinical use is still limited. At least two major hurdles need to be addressed to stimulate widespread clinical usage. For many methods, the excessive scan time associated with the measurement of the three parameters has so far prohibited its clinical application. However, in recent years there has been substantial progress (see, e.g., Refs. 2–14) and the method here presented allows for absolute quantification of  $T_1$ ,  $T_2$ , PD, and the  $B_1$  inhomogeneity of a whole volume with high resolution in a mere 5 min. The second hurdle, which must not be underestimated, is the clinical evaluation of the images. So far, there is only limited experience in using absolute  $T_1$ ,  $T_2$ , and PD maps in clinical routines and most radiologists will want to confirm their findings using conventionally-weighted contrast images. The quantification scan might then be considered as superfluous in the limited time available for an examination. This item is addressed using the approach of synthetic MRI (15–20). It is possible to synthesize any  $T_1$ -weighted or  $T_2$ -weighted contrast image based on the absolute parameters, by calculating the expected image intensity as a function of a virtual set of scanner settings. Synthetic MRI can be seen as a translation of the absolute maps into conventional contrast images; thus, a single quantification scan can provide both the absolute maps and the contrast images for the examination.

A recently published work explained a method that enabled rapid, simultaneous quantification of  $T_1$ ,  $T_2^*$ , PD, and  $B_1$  field, called QRAPTEST (2). The current work presents a substantially improved method that has been optimized to accommodate clinical use, dubbed “Quantification of Relaxation Times and Proton Density by Multiecho acquisition of a saturation-recovery using Turbo spin-Echo Readout” (QRAPMASTER). Two main issues of the QRAPTEST method were addressed. First, a spin-echo sequence is used rather than a gradient-echo sequence. In routine clinical practice, spin-echo sequences are most commonly used due to their insensitivity to susceptibility effects. These are caused by  $B_0$  inhomogeneities in the volume of interest, leading to a  $T_2^*$  relaxation in gradient-echo imaging where  $T_2^*$  is shorter than  $T_2$ . This may result in image blurring of the tissue interfaces at longer echo times. Second, the maximum excitation flip angle for the

<sup>1</sup>Center for Medical Imaging Science and Visualization (CMIV), Linköping University, Linköping, Sweden.

<sup>2</sup>Division of Clinical Physiology, Department of Medicine and Health, University Hospital, Linköping, Sweden.

<sup>3</sup>Synthetic MR Technologies AB, Stockholm, Sweden.

<sup>4</sup>Divisions of Radiation Physics and Radiology, Department of Medicine and Health, University Hospital, Linköping, Sweden.

Grant sponsors: University Hospital Research Funds; Medical Research Council of Southeast Sweden.

\*Correspondence to: J.B.M. Warntjes, Center for Medical Imaging Science and Visualization (CMIV), Linköping University, SE58185 Linköping, Sweden. E-mail: Marcel.warntjes@cmiv.liu.se

Received 5 October 2007; revised 26 February 2008; accepted 28 February 2008.

DOI 10.1002/mrm.21635

Published online in Wiley InterScience (www.interscience.wiley.com).

© 2008 Wiley-Liss, Inc.

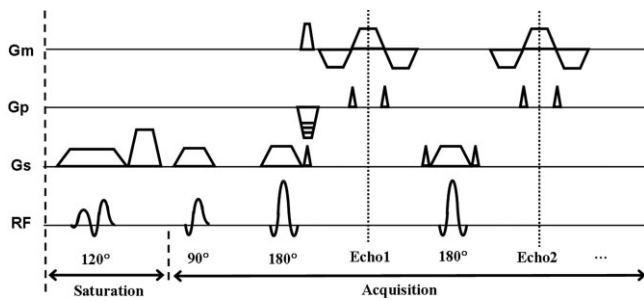


FIG. 1. Schematic representation of a single block of the QRAPMASTER quantification sequence. Shown are the measurement ( $G_m$ ), phase-encoding ( $G_p$ ), and slice-selection ( $G_s$ ) gradients and the RF pulse amplitude over time. There are two phases in each block. In phase 1 (saturation), the  $120^\circ$  saturation pulse  $\theta$  and subsequent spoiling acts on a slice  $m$ . In phase 2 (acquisition), the multiecho spin-echo acquisition is performed on slice  $n$ , using the  $90^\circ$  excitation pulse  $\alpha$  and multiple  $180^\circ$  refocusing pulses. The spin-echo acquisition is accelerated with an EPI readout scheme.

QRAPTEST acquisition was typically limited to  $4\text{--}8^\circ$  due to its role as a correction factor in the calculation of  $T_1$  relaxation. The QRAPMASTER approach uses a multislice sequence with a long repetition time between subsequent acquisitions, removing the limitation of the flip angle. The method presented is very signal efficient, and accurate values of the absolute MR parameters with a large dynamic range over a complete volume can be obtained within the desired 5-min benchmark.

## MATERIALS AND METHODS

### General Sequence Design

A basic block of the quantification sequence is shown in Fig. 1, with two phases in each block, repeated over the complete measurement. In the first phase a slice selective saturation pulse  $\theta$ ; acts on a slice  $n$ , followed by spoiling of the signal ("saturation"). In the second phase a slice-selective spin echo acquisition of another slice  $m$  ("acquisition"), consisting of multiple echoes that are acquired to measure the transverse relaxation time  $T_2$ , is performed. The acquisition can be accelerated through an echo-planar imaging (EPI) technique that acquires several  $k$ -space lines per spin-echo (gradient spin-echo or GRaSE). The advantage of this technique is to simultaneously reduce the specific absorption rate (SAR) of the measurement, making it attractive for high-field applications. The number of echoes and the echo spacing can be freely chosen to accommodate any dynamic range for the measurement of  $T_2$ .

By shifting the order of the slices  $n$  and  $m$  with respect to each other, the desired delay time between saturation and acquisition of a particular slice can be set. By using different delay times, the longitudinal relaxation time  $T_1$  after a saturation pulse is retrieved from multiple scans. Since the number of scans and the delay times can be freely chosen, the dynamic range of  $T_1$  can also be set as desired. The freedom to choose the number of data points on the  $T_1$  curve is an important difference compared to previously described multislice methods, where the number of data points are determined by the number of slices

(e.g., Refs. 8 and 9). An important feature of the QRAPMASTER approach is that  $T_1$  and  $T_2$  maps are measured independently of each other and hence no error propagation can occur between the two. The sequence is very signal effective, the duty cycle of the receivers is approximately 50% to 60% of the total scan time, and there is no limit on the acquisition flip angle. By using a saturation pulse rather than a more common inversion pulse, another very significant advantage is the possibility to simultaneously measure the local  $B_1$  field, as will be explained later. Based on  $T_1$ ,  $T_2$ , and  $B_1$  it is possible to retrieve the unsaturated magnetization  $M_0$ , which can be scaled to the PD.

The sequence results in black-blood imaging due to the constant saturation of flowing blood. A "regional saturation" (REST) pulse was added, located parallel to the imaging volume, to avoid a difference in behavior of the first and last slices.

### Pulse Profile Simulation

To correct for the nonideal behavior of the slice-selective RF pulses on the quantification results, as well as to relate the observed saturation flip angle  $\theta_{\text{eff}}$  to the effective excitation flip angle  $\alpha_{\text{eff}}$ , a spin system simulation of the complete sequence was performed. RF pulse simulations are excellently described in Ref. 21, where a geometrical system of magnetic spins was defined with the macroscopic longitudinal magnetization  $M_z = 1$  and the transverse magnetization  $M_{xy} = 0$ . The amplitude envelopes of the  $120^\circ$  saturation,  $90^\circ$  excitation, and  $180^\circ$  refocusing pulses of the quantification measurement were obtained from the MR scanner software.

The envelopes were approximated as a set of RF block pulses of  $1\text{-}\mu\text{s}$  unit time. The effect of the separate RF block pulses on the spin system was sandwiched with the effect of the simultaneously applied gradient field during a unit time. The complete quantification scan was simulated for each individual magnetic spin. The  $120^\circ$  saturation pulse was applied, rotating the spins around the  $y$  axis, and the resulting transverse magnetization  $M_{xy}$  was spoiled with a strong  $z$ -gradient. After a delay of between 0 ms and 4000 ms a spin-echo acquisition was performed, during which a  $T_1$  relaxation of the magnetization was allowed, using  $T_1 = 1000$  ms. The spin-echo acquisition consisted of the  $90^\circ$  excitation pulse, rotating the spins around the  $y$  axis, and a series of  $180^\circ$  refocusing pulses, rotating the spins around the  $x$  axis, together with gradient winders and rewinders. The macroscopic signal intensity was obtained as the integral of the  $x$ -component of the transverse magnetization  $M_x$  of the spins.

### Extraction of the Parameters

The complete quantification measurement consists of numerous scans with different delay times  $T_D$ , providing a  $T_1$  relaxation curve after the saturation pulse. The steady-state magnetization  $M_{TD}$  at a specific delay time  $T_D$  can be found using the recursive relation of magnetization over the repetition time  $T_R$ , using an excitation pulse  $\alpha$  and the steady-state magnetization  $M_{TR}$  at the end of  $T_R$ , just before the subsequent saturation pulse:

$$M_{TD} = M_0 - (M_0 - M_{TR} \cos \theta) \exp(-T_D/T_1) \quad [1]$$

$$M_{TR} = M_0 - (M_0 - M_{TD} \cos \alpha) \exp(-(T_R - T_D)/T_1), \quad [2]$$

where  $M_0$  is the unsaturated magnetization. Substituting Eq. [2] into Eq. [1], the magnetization  $M_{TD}$  as a function of delay time  $T_D$  after the saturation pulse becomes:

$$M_{TD} = M_0 \frac{1 - (1 - \cos \theta) \exp(-T_D/T_1) - \cos \theta \exp(-T_R/T_1)}{1 - \cos \theta \exp(-T_R/T_1) \cos \alpha}. \quad [3]$$

Hence, from the measured intensity at various delay times a fit can be performed to retrieve both  $T_1$  and  $M_0$ . Furthermore, from the same  $T_1$  relaxation curve the effective local saturation flip angle  $\theta_{\text{eff}}$  can be found, and thus the local  $B_1$  field. This is done using the ratio between the magnetization  $M_{T0}$  at time 0, just after the saturation pulse, and  $M_{TR}$  at time  $T_R$ , just before the subsequent saturation pulse:

$$\theta_{\text{eff}} = \arccos(M_{T0}/M_{TR}), \quad [4]$$

since the difference between  $M_{T0}$  and  $M_{TR}$  is entirely due to the effect of the saturation pulse and subsequent spoiling. Based on the observed  $\theta_{\text{eff}}$ , the actual local excitation flip angle  $\alpha_{\text{eff}}$  can be estimated as well, though this is not as straightforward because it requires knowledge of the RF pulse profiles and the actual spin behavior in a particular  $B_1$  field. A simulation was performed to relate  $\theta_{\text{eff}}$  to  $\alpha_{\text{eff}}$  (see below).

As previously mentioned, each acquisition is performed using a multiecho readout that enables the simultaneous measurement of  $T_2$  relaxation. Using  $T_2$  and the fitted  $M_0$  from the  $T_1$  curve, the intensity  $S_{M0}$ , proportional to  $M_0$  at an echo time zero, can be retrieved. Proton density is then calculated from  $S_{M0}$ , including a number of scaling factors according to:

$$PD = C_{\text{coil}} C_{\text{load}} C_{\text{vol}} C_{\text{pix}} C_{\text{temp}} C_{\text{arb}} \frac{S_{M0}}{\sin(\alpha_{\text{eff}}) \alpha_{\text{eff}}}, \quad [5]$$

where  $C_{\text{coil}}$  is a scaling factor for the local sensitivity of the applied receive coil,  $C_{\text{load}}$  is a scaling factor for load differences of the quadrature body coil (QBC),  $C_{\text{vol}}$  is a scaling factor to a 1-mm<sup>3</sup> unit voxel volume,  $C_{\text{pix}}$  is the scaling factor from image pixel values to MR absolute intensity values,  $C_{\text{temp}}$  is a scaling factor for temperature differences between different measurements (phantoms vs. humans), and  $C_{\text{arb}}$  is an arbitrary rescaling factor to display more convenient values. For more details see Ref. 2.

### Fitting Algorithm

The fitting routine was performed as follows. The phase of the last dynamic echo images was used as a reference phase. For all other images this phase is subtracted to generate real images instead of modulus, identical to the phase-sensitive method (22). This removes the ambiguity of the signal sign that occurs in modulus images. The noise

behavior of the resulting images is Gaussian rather than Rician, removing the potential overestimation of signal intensity at low signal strength.

A monoexponential  $T_2$  relaxation was retrieved from all images in which the absolute intensity served as a weight in the least-square fit. The expected intensity at an echo-time of zero was subsequently calculated for all time points. Using this procedure all echo-images are projected onto a single  $T_1$  curve at echo-time zero. The saturation flip angle  $\theta_{\text{eff}}$  was calculated according to Eq. [4] from this curve. Since the  $B_1$  field was assumed to not change rapidly over the volume, a median filter of 10 mm was applied. A least-square fit on the  $T_1$  curve results in an estimate of  $T_1$  and  $M_0$ . In this fit,  $M_{T0} = M_{TC} \cos \theta$  was taken as an additional condition. Finally,  $M_0$  was scaled to proton density.

### Synthetic MRI

Using the approach of synthetic MRI, it is possible to create contrast-weighted images based on the quantified data using the well-known equations that describe MR intensity as a function of scanner settings, such as  $T_E$ ,  $T_R$ , and flip angle  $\alpha$ , in relation to  $T_1$ ,  $T_2$ , and PD (21).

$$S \propto PD \frac{1 - \exp(-T_R/T_1)}{1 - \exp(-T_R/T_1) \cos \alpha} \exp(-T_E/T_2). \quad [6]$$

Inversion-recovery images (e.g., fluid attenuation inversion recovery [FLAIR]) can be calculated using the inversion delay time,  $T_{IR}$ , according to

$$S \propto PD \left[ \frac{1 - 2 \exp(-T_R/T_1) + \exp(-T_R/T_1)}{1 + \exp(-T_R/T_1) \cos \alpha} \right] \exp(-T_E/T_2). \quad [7]$$

Since  $T_E$ ,  $T_R$ ,  $\alpha$ , and  $T_{IR}$  are independent parameters, any contrast image can be synthesized.

The fitting and visualization of the quantification data, as well as the calculation and the visualization of the synthesized MR images, were done using an in-house developed software program based on IDL (Research Systems Inc, Boulder, CO, USA). Fitting a full data set requires on the order of 20 s on a Pentium III computer.

### Sequence Details

All experiments were performed on a 1.5T Achieva scanner (Philips Medical Systems, Best, The Netherlands). The longitudinal magnetization after a saturation, an excitation pulse, and a refocusing pulse, and thus their effective flip angles as a function of slice distance, were determined by applying either of these pulses, followed immediately by gradient spoiling and acquisition perpendicular to the slice. This was done using an agar phantom with  $T_1$  relaxation of 380 ms (previously determined) with a repetition time of 3 s. The observed intensity was corrected for the 10-ms delay between the center of the RF pulses and the start of the actual acquisition. The intensity was normalized by repeating the measurement with the RF amplitude set to zero.



For the clinical scan, five spin echoes were acquired using an EPI factor of 3 at multiples of 20-ms echo time. The resulting acquisition time per sequence block (Fig. 1) was 130 ms.  $T_R$  was set to minimum, which for the 20 slices was 2600 ms. Four dynamic scans were performed, with delay times between the saturation pulse and acquisition of 130, 390, 1170, and 2470 ms. The matrix size was  $270^2$  over a field of view of 215 mm, leading to an in-plane resolution of 0.8 mm, reconstructed to 0.75 mm. Further acceleration was achieved using a sensitivity encoding (SENSE) factor of 2, leading to a scan time of 5:14 min:s. To ensure steady-state conditions a single dummy acquisition was performed across all slices prior to each dynamic and the delay times were performed in reversed order. In addition, an 80-mm REST slab was located at the neck of the patient to suppress blood flow artifacts. To avoid potential errors in the measured  $T_1$  curves due to slice cross-talk, the slice order of the quantification scan was chosen linearly, such that the error would become similar for each slice. In our view, this is a better approach than a standard interleaved slice order that could lead to a varying error of the  $T_1$  curves per slice.

The QRAPMASTER sequence was compared to the golden standard methods for quantification. The  $T_1$  relaxation was measured using the standard inversion-recovery sequence, a single-slice spin-echo with  $T_R = 10$  s and  $T_{IR} = 100, 400, 700, 1500$ , and 5000 ms. The  $T_2$  relaxation was measured using a three-dimensional (3D) multiecho sequence with 15 spin echoes at intervals of 15 ms and  $T_R = 3$  s. The  $B_1$  field was retrieved using a flip angle sweep of a 3D gradient-echo sequence with  $T_R = 8$  s and flip angles at 30, 50, 70, 90, and 120°. A sinus wave was fitted to the resulting intensity to retrieve the  $B_1$  values.

To examine a patient with clinically definite multiple sclerosis (CDMS),  $T_1$ -weighted images ( $T_R = 590$  ms,  $T_E = 15$  ms, resolution = 0.8 mm) and the QRAPMASTER quantification scan were acquired. Gadolinium contrast agent was administered (Magnevist; Schering, Germany), followed by the acquisition of  $T_2$ -weighted images ( $T_R = 4400$  ms,  $T_E = 100$  ms, resolution = 0.6 mm) and  $T_2$ -weighted FLAIR images ( $T_R = 6000$  ms,  $T_E = 120$  ms,  $T_{IR} = 2000$  ms, resolution = 0.8 mm). Finally, a second acquisition of the  $T_1$ -weighted images and the quantification scan was performed. For comparison, 10 healthy volunteers were investigated with the QRAPMASTER scan using a lower SENSE acceleration factor, which led to a scan time of 8:35 min:s. All in vivo studies were performed in compliance with the regulations of Swedish law.

## RESULTS

### Effect of the RF Pulse Profiles

The 90° excitation, 120° saturation, and 180° refocusing pulse were measured as described in Materials and Methods. The effective RF pulse flip angle in Fig. 2 is displayed as a function of distance across the slice, normalized to slice thickness, where 100 data points were measured per unit. The solid lines represent the simulation of the pulse angles based on their amplitude envelope over time and their associated gradients. To aid visual inspection, the ideal slice-selective 90°, 120°, and 180° RF pulse angles are

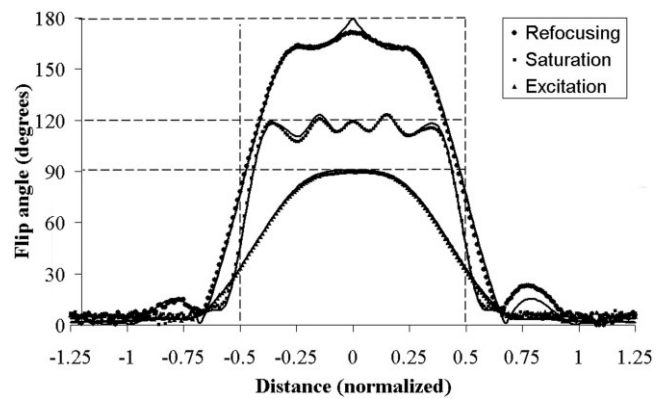


FIG. 2. The measured effective flip angle of the nominal 90° excitation pulse  $\alpha$ , the nominal 120° saturation pulse  $\theta$ , and the nominal 180° refocusing pulse as a function of normalized slice thickness. The solid lines are the simulated flip angles based on the RF amplitude profile of the nonideal pulses. The dashed lines indicate the effect of ideal slice-selective RF pulses.

shown as dashed lines. As can be seen in Fig. 2, the ideal flip angle was only achieved at exactly the resonance in the center of the slice. Generally, all other frequencies have lower effective flip angles. Furthermore, there was a slight nonzero flip angle outside the intended slice thickness. The simulations of the RF pulses agree very well with the measured data, with only the central peak of the refocusing pulse not entirely resolved in the measurement.

The quantification sequence was simulated for each point in Fig. 2, using the actual nonideal RF pulse profiles. The x-component of the transverse magnetization  $M_x$  was integrated over the complete slice distance of Fig. 2 to reflect the signal intensity of the measurement. If ideal slice-selective RF pulses were used, the observed normalized intensity as a function of delay time would correspond to the dotted line in Fig. 3. The line starts at  $\cos(120^\circ) = -0.5$  and approaches unity at infinite times after the saturation pulse. However, the intensity of all spin-echo readouts begins at  $-0.26$  when using the nonideal pulse profiles. There is a long delay after the saturation pulse, the first spin-echo readout intensity approaches 0.899, the second spin-echo readout approaches 0.954, and all subsequent spin-echo readouts approach a value close to the average intensity of 0.932.

The simulation showed that the signal obtained from the measurement reflects the actual  $T_1$  decay, but will appear to be associated with both a lower effective saturation angle and a lower effective excitation angle than the intended nominal values. Using Eq. [4], the effective saturation pulse angle of the intensity curve of Fig. 3 was calculated to be  $106^\circ$  ( $\cos(-0.26/0.932)$ ) rather than the nominal 120°. From the first 10 spin-echo readouts, the effective excitation pulse angle  $\alpha_{\text{eff}}$  (where  $\int M_x = \int M_z \sin(\alpha_{\text{eff}})$ ) of the first readout corresponds to  $64.0^\circ$ , the second readout corresponds to  $72.6^\circ$ , and the average readout corresponds to  $68.7^\circ$ , rather than the nominal 90°.

The simulation was repeated for a number of different  $B_1$  field strengths. The  $B_1$  field varies across a patient, and the intended saturation and excitation pulse amplitudes thus vary accordingly. In Fig. 4a, the observed effective satura-

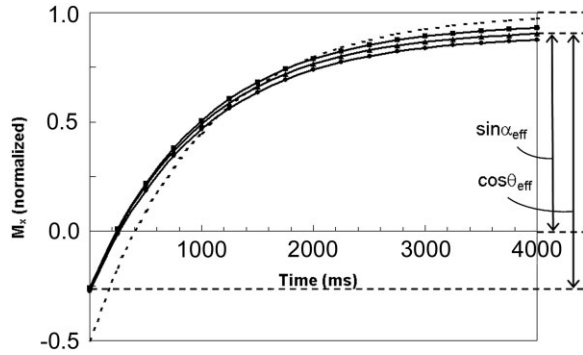


FIG. 3. The simulated signal intensity of the measurement on a phantom with  $T_1 = 1000$  ms. The longitudinal magnetization is initialized to unity for a completely relaxed system. A  $120^\circ$  saturation pulse is applied at time 0. The normalized signal intensity of a multiecho spin-echo acquisition is plotted, performed at a time between 0 and 4000 ms. The dotted line indicates the ideal behavior. The solid lines are the echo intensities using the imperfect RF pulses as shown in Fig. 2. The first echo has a lower intensity and the second spin-echo has a higher intensity than the average intensity of the first 10 echoes. The arrows indicate the calculation of  $\sin(\alpha_{\text{eff}})$  and  $\cos(\theta_{\text{eff}})$  from these curves.

tion pulse angle is shown as a function of the nominal saturation pulse angle. In Fig. 4b, the observed effective excitation pulse angle is shown as a function of the nominal excitation pulse angle. The dashed lines indicate the intended  $B_1$  field.

The RF pulse simulations were also used to investigate the potential problem of cross-talk between slices, leading to a through-plane smoothing of the input data for the quantification. The simulation showed that the contribution of the signal outside a slice was about 7% of the total signal. Introducing a gap of 10% of the slice thickness between the slices reduced the amount to 3%.

#### Modification of the Fitting Algorithm

Based on the simulation results two modifications were incorporated into the fitting algorithm. First, the measured

intensities of each first and second echo were corrected. The intensity of the first echo was multiplied by a factor of 1.036 and the intensity of the second echo was multiplied by a factor of 0.977, such that the effective excitation angle became  $68.7^\circ$  for all spin-echo readouts at nominal  $B_1$  field. This correction significantly improved  $T_2$  estimation, since the method only uses a relatively low number of spin-echo readouts.

Second, the measured effective saturation pulse angle was related to the effective excitation pulse by combining Fig. 4a and b into Fig. 4c, where the effective excitation pulse angle  $\alpha_{\text{eff}}$  was plotted as a function of effective saturation pulse angle  $\theta_{\text{eff}}$ . With this diagram the observed saturation angle from the measurement can be converted into the effective excitation angle that was used to calculate the proton density (Eq. [5]). As seen from Fig. 4c, the relation between the pulse angles can be approximated by a simple  $\alpha_{\text{eff}} = (\theta_{\text{eff}} - 34.5^\circ) < 69^\circ$ . This empiric equation is applicable for values of  $\theta_{\text{eff}}$  in the range  $80^\circ$ – $115^\circ$ , corresponding to a  $B_1$  field inhomogeneity between 70% and 110%. Cross-talk between slices due to pulse profile imperfections were ignored for the quantification.

#### In Vivo Measurements on Volunteers

Absolute quantification of  $T_1$ ,  $T_2$ , and PD was performed on 10 healthy volunteers (mean age = 29 years, eight male, two female). Table 1 summarizes the normal values for various anatomies of the brain. These values correspond well with those from the literature. Note that the average values of white matter (WM) vary smoothly across the brain,  $T_1$  is shorter in the frontal part of the brain than in the occipital part and  $T_2$  is slightly higher in the center of the brain. The thalamus showed different values across the tissue and the values of its center were chosen for Table 1. Most voxels containing cortical gray matter are affected by partial volume effects with nearby cerebrospinal fluid (CSF) or WM, and the intrinsic absolute values are difficult to retrieve. The proton density of CSF appears somewhat high, possibly due to flow-effects or diffusion. In spite of these notions, the average values fall within a relatively narrow range.

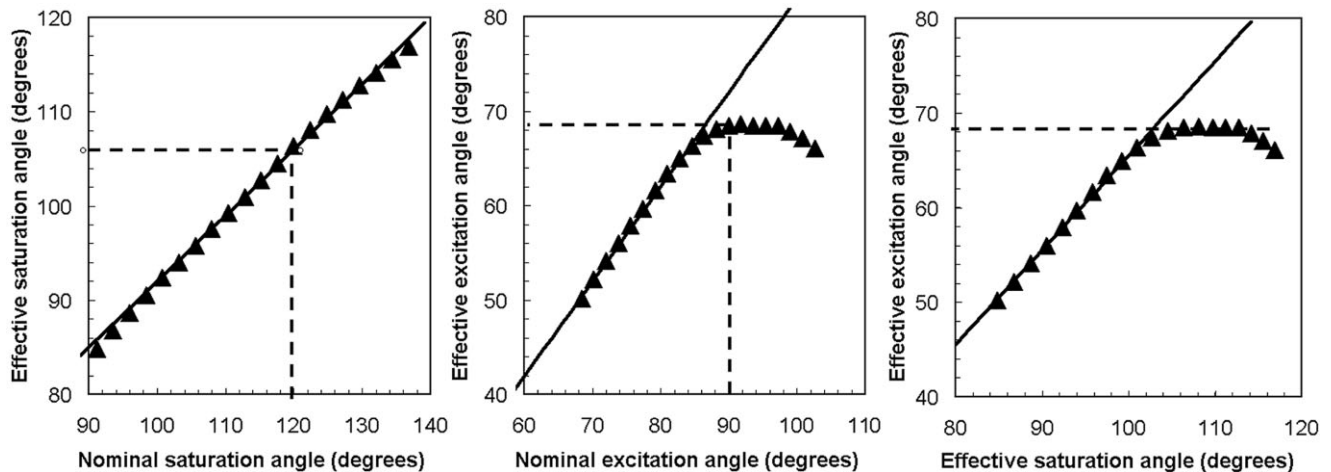


FIG. 4. **a:** Simulation of the relation of the nominal saturation flip angle  $\theta$  and the observed effective saturation flip angle  $\theta_{\text{eff}}$ , based on the fitting of the  $T_1$  curves of the quantification measurement shown in Fig. 3. **b:** Similar to the nominal excitation flip angle  $\alpha$  and the effective excitation flip angle  $\alpha_{\text{eff}}$ . **c:** The observed effective saturation flip angle  $\theta_{\text{eff}}$  related to the effective excitation flip angle  $\alpha_{\text{eff}}$ .

Table 1

Average  $\pm$  SD of  $T_1$  and  $T_2$  Relaxation Times and Proton Densities in the Brain of 10 Healthy Volunteers (First Column) Compared With Published Values (Second Column)

Anatomy	$T_1$ (ms) <sup>a</sup>	$T_2$ (ms) <sup>a</sup>	PD <sup>a,b</sup>
Frontal white matter	561 $\pm$ 12	568 $\pm$ 27 (4); 585 $\pm$ 33 (6)	73 $\pm$ 2
Occipital white matter	589 $\pm$ 19	592 $\pm$ 21 (4); 610 $\pm$ 30 (6)	77 $\pm$ 5 (12)
Genu	556 $\pm$ 15	543 $\pm$ 25 (4); 572 $\pm$ 35 (6)	78 $\pm$ 3
Splenium	598 $\pm$ 11	565 $\pm$ 17 (4); 569 $\pm$ 38 (6)	71 $\pm$ 1 (13)
Cortex	1048 $\pm$ 61	1260 (13)	82 $\pm$ 7
Thalamus	738 $\pm$ 39	782 $\pm$ 19 (4)	82 $\pm$ 1 (13)
Putamen	832 $\pm$ 25	854 $\pm$ 13 (4); 950 $\pm$ 90 (6)	76 $\pm$ 2
Head of the caudate nucleus	917 $\pm$ 43	924 $\pm$ 28 (4); 1035 $\pm$ 65 (6)	74 $\pm$ 1 (13)
CSF	3940 $\pm$ 340	3700 $\pm$ 500 (9)	1910 $\pm$ 520
			1029 $\pm$ 26
			970 (14)

<sup>a</sup>Numbers in parentheses are reference citations.

<sup>b</sup>Where the PD of pure water at 37°C corresponds to 1000.

For validation, the clinical QRAPMASTER sequence results of a single slice of the brain from a healthy volunteer were compared to the golden standard methods for  $T_1$ ,  $T_2$ , and  $B_1$ . Combining these three methods also retrieved the PD. Figure 5a displays the  $T_1$  relaxation measured by QRAPMASTER and Fig. 5b displays the relaxation measured by the reference standard inversion-recovery. The scaling is 0 ms to 2000 ms. There is clearly a significant blurring in Fig. 5b caused by movement of the volunteer

over the total acquisition time of 19 min of the inversion-recovery images. The cortex appears thicker and the ventricles show an edge artifact. Regions of interest (ROIs) were placed at various locations. The measured values of all pixels within the ROIs of the reference  $T_1$  measurement were plotted in Fig. 5c as a function of the measured values using QRAPMASTER. The scale for the relaxation times is logarithmic. Most regions are in excellent agreement. For CSF, there is a significant spread of measured

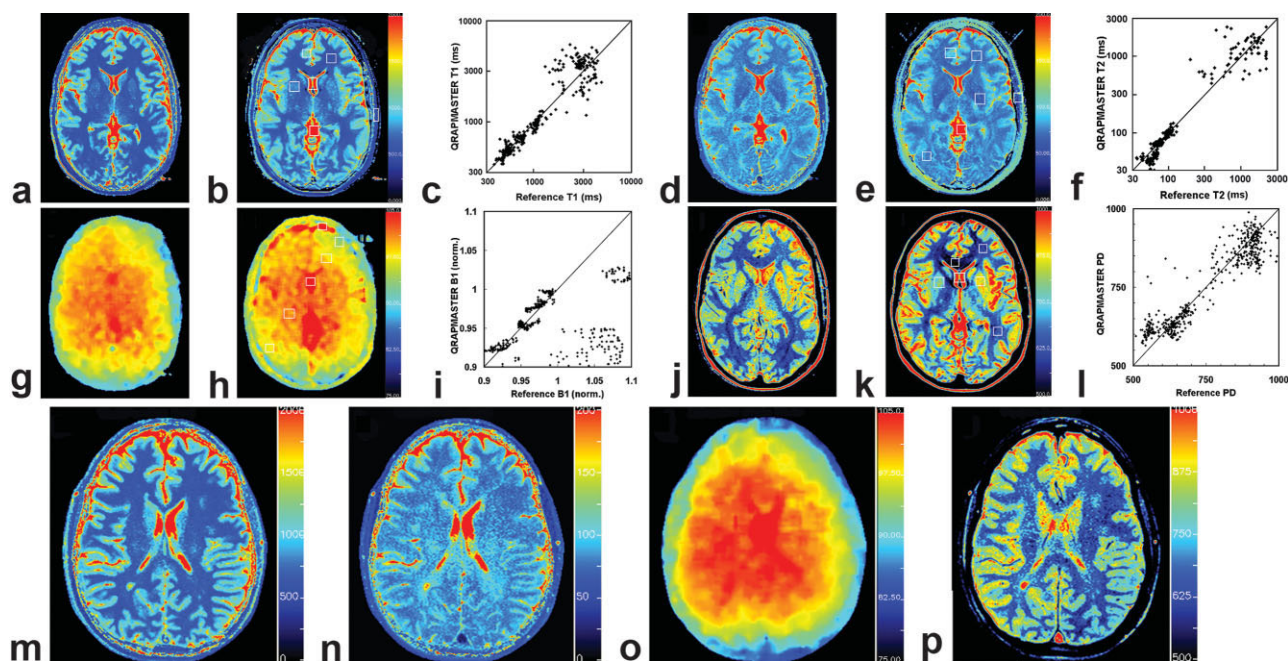


FIG. 5. Application of the QRAPMASTER method on the brain. In-plane resolution = 0.8 mm, slice thickness = 5 mm, and 20 slices are acquired in a scan time of 5.14 min. The values of the longitudinal  $T_1$  relaxation (ms) obtained (a) by QRAPMASTER and (b) by the reference standard inversion-recovery. c: The comparison of the two methods of all pixels inside the indicated ROIs. d–f: Similar to the transverse  $T_2$  relaxation compared to a standard 3D multiecho sequence; (g–i) similar to the  $B_1$  field compared to the standard flip angle sweep method; and (j–l) similar to the PD compared to all reference methods combined. m–p: Application of the quantification method on a patient with MS.



values. This is caused by partial volume effects at the tissue interface of CSF with WM, where values are sensitive to the slightest, subpixel-sized, misregistration between the two sequences. To avoid this effect, most ROIs were placed in more or less homogeneous regions. The mean difference for the ROIs, excluding CSF, was 6.2%.

Similarly, the results of the same QRAPMASTER measurements were compared to the multiecho sequence (scan time = 5 min) in Fig. 5d–f. The scaling is 0 ms to 200 ms. The  $T_2$  values obtained by both methods were very similar, with a mean difference of 5.2% (excluding CSF), mainly caused by the difference in the values of subcutaneous fat (42 ms using QRAPMASTER vs. 51 ms for the reference method). A comparison with the flip angle sweep method is shown in Fig. 5g–i. Both images were median smoothed over 10 mm. Still, movement artifacts in the 13-min scan time and insufficient magnetization-recovery in the 8-s repetition time led to incorrect values for CSF using the flip angle sweep method, as seen from the large cloud of data points to the right side of the plot in Fig. 5i. It is also clear that the standard deviation (SD) of the values from the reference method is much larger than those of the QRAPMASTER method, despite a longer scan time.

All reference methods were combined to calculate the proton density of the axial slice. The comparison is displayed in Fig. 5j–l. The scaling is 500–1000 for PD, where 1000 corresponds to pure water at 37°C. All errors in the previous parameters propagate to PD and the combined reference methods, with a total scan time of 37 min, result in only a moderately accurate image (Fig. 5k). The mean difference of the values in Fig. 5l is 12.1%.

#### In Vivo Measurements on a Patient With MS

The quantification method was applied to a patient with CDMS, both before and after the administration of Gd contrast media. The post-Gd absolute MR tissue parameters  $T_1$ ,  $T_2$ ,  $B_1$ , and PD of a transversal slice of the patient's brain are shown in Fig. 5m–p, and are similar to Fig. 5a, d, g, and j, respectively. The administration of Gd did not result in significant differences in relaxation times, indicating the absence of blood-brain-barrier leakage. The cortical tissue of the patient had an average  $T_1$  relaxation of  $1022 \pm 45$  ms before and  $998 \pm 47$  ms after Gd, and a  $T_2$  relaxation of  $87 \pm 4$  ms both before and after Gd, and the PD =  $880 \pm 35$ . For frontal WM, these values were  $T_1 = 598 \pm 34$  and  $T_2 = 70 \pm 4$  before Gd,  $T_1 = 578 \pm 36$  and  $T_2 = 68 \pm 5$  after Gd, and the PD =  $670 \pm 21$ .

Figure 6 shows the  $T_2$ -weighted and  $T_2$ -weighted-FLAIR images together with the  $T_1$ -weighted image of the axial slice after administration of Gd contrast. The top panel (Fig. 6a–c) shows the conventionally acquired images, and the bottom panel (Fig. 6d–f) displays the corresponding synthetic contrast images, based on the data shown in Fig. 5m–p. The synthetic MR images were calculated using identical scanner settings as the conventional images. Upon visual inspection, there is excellent agreement in contrast appearance between conventional and synthetic images, both for normal tissue and pathology. The mean difference between the conventional and synthetic  $T_2$ -weighted images is 17%, FLAIR images is 16% and  $T_1$ -weighted images is 18%. These large differences, however,

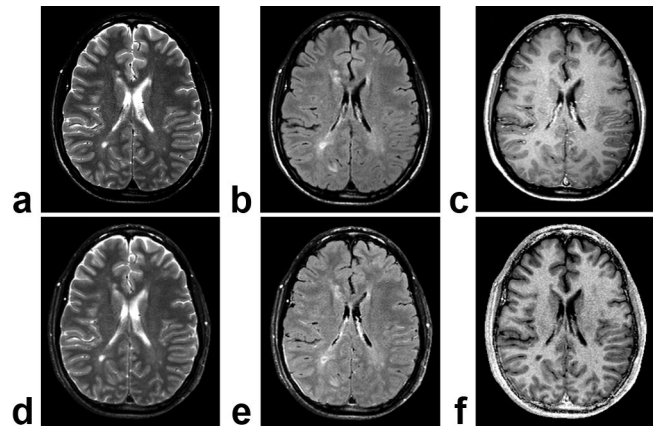


FIG. 6. Contrast images of the identical slice as shown in Fig. 5. The patient moved slightly over the various scans. The top row was acquired conventionally, the bottom row was synthesized based on the quantified data displayed in Fig. 5. (a,d)  $T_2$ -weighted image ( $T_R = 4400$  ms,  $T_E = 100$  ms,  $\alpha = 90^\circ$ ), (b,e)  $T_2$ -weighted FLAIR image ( $T_R = 6000$  ms,  $T_E = 120$  ms,  $T_{IR} = 2000$  ms,  $\alpha = 90^\circ$ ), and (c,f)  $T_1$ -weighted image 5 min after the administration of Gd contrast media ( $T_R = 550$  ms,  $T_E = 15$  ms,  $\alpha = 90^\circ$ ).

are mainly due to the variation in signal intensity of the subcutaneous fat and the skull in the images. If the brain is segmented, the mean differences are 10% for  $T_2$ -weighted images, 7% for FLAIR images and 9% for  $T_1$ -weighted images. The most striking difference between the images is the appearance of blood in the  $T_1$ -weighted image. In the conventional  $T_1$ -weighting, the blood is Gd enhanced, whereas it is strongly suppressed in the synthetic  $T_1$ -weighting since the quantification sequence results in black blood.

To visualize the quantification results for the  $T_2$  hyper-enhancement of the patient, the three measured parameters were used as coordinates in a Cartesian  $R_1$ - $R_2$ -PD space, where the longitudinal relaxation rate  $R_1 = 1/T_1$  and the transverse relaxation rate  $R_2 = 1/T_2$ . All tissues then group into characteristic clusters. Voxels containing a mixture of two different kinds of tissues appear on a straight line between both clusters. The position on this line is a weighted average of the partial volume of the corresponding tissue types. Figure 7 shows a scatter plot of such a visualization from a small portion of the brain from a healthy volunteer, indicated by the ROI in the  $T_2$ -weighted image (inset). Only the projection of  $R_1$ - $R_2$ -PD space onto the  $R_1$ - $R_2$  plane is shown. The tissue clusters of WM, cortex, and CSF are clearly observed, as well as the voxels containing both tissue types. The amount of CSF in the gyri inside the ROI is so small that there are no voxels present consisting entirely of CSF. The reference positions of the separate clusters were obtained from Table 1 and are highlighted by the gray circles in Fig. 7. The patient with MS is similarly visualized in Fig. 8. It can be observed from the data points that MS lesions have distinctively different values than normal tissue on this  $R_1$ - $R_2$  plot. Lesions even seem to have two distinct phases, as indicated by the two gray lines over the data points. In the first phase, there is a differentiation from normal WM with a significant reduction in  $R_2$ , from WM  $R_1 = 1.75$  s $^{-1}$  and

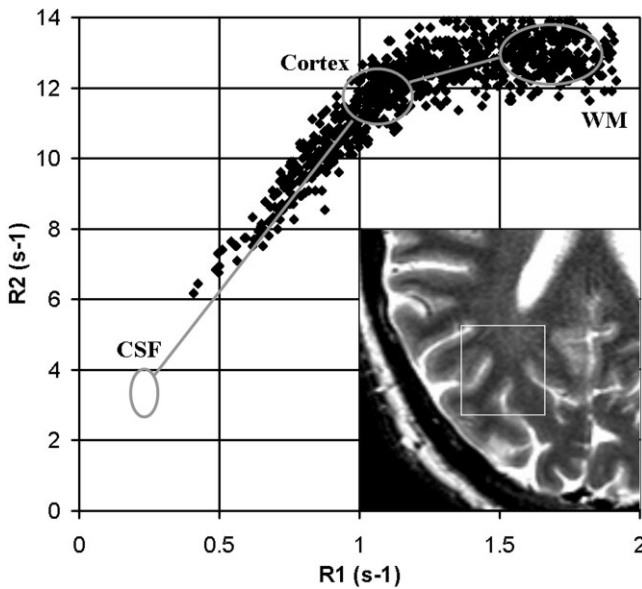


FIG. 7. Projected scatter plot of the absolute values of a small part of the brain of a healthy volunteer indicated by the ROI in the  $T_2$ -weighted image (inset). The relaxation rate  $R_2$  is shown as a function  $R_1$ . The cluster positions of WM, cortex, and CSF, are highlighted based on the values of Table 1.

$R_2 = 13.3 \text{ s}^{-1}$  toward  $R_1 = 1.54 \text{ s}^{-1}$  and  $R_2 = 10.5 \text{ s}^{-1}$  ( $T_1 = 650 \text{ ms}$  and  $T_2 = 95 \text{ ms}$ ), indicated by the first gray dot. Simultaneously, the water content increases slightly, from 650 to 680. This affected area covers about one-quarter of the ROI around the hyperintense spot in the  $T_2$ -weighted image. Although these changes are significant they only show up as faint white areas in the  $T_2$ -weighted and  $T_2$ -weighted-FLAIR images and might not be considered for diagnosis. The actual hyperenhanced spots on the contrast images consist of a dramatic increase in all three parameters, representing the second phase in the lesion data of Fig. 8. The water content has increased to 1000 at  $R_1 = 0.61 \text{ s}^{-1}$  and  $R_2 = 5.88 \text{ s}^{-1}$  ( $T_1 = 1650 \text{ ms}$  and  $T_2 = 170 \text{ ms}$ ), indicated by the second gray dot. At this position the destruction of WM appears to be complete and is replaced by liquid. The relaxation rates of a lesion might even be lower, though this appears more to reflect the composition of the lesional liquid. The development of MS lesions over these two phases is in line with the observation of enhanced intensity on a FLAIR image at an early stage, and a darker appearance at a later stage of the lesioning process.

## DISCUSSION

As shown in the results, absolute values for the longitudinal  $T_1$  relaxation, the transverse  $T_2$  relaxation, the PD, and the local radio frequency  $B_1$  field can be determined within a clinically acceptable time of 5 min, covering the complete brain at high resolution. A significant strength of the presented QRAPMASTER method is that it not only measures all relevant MR parameters simultaneously, such that the acquired signal is utilized for an accurate estimation of the complete set of parameters, it also includes an intrinsic correction for  $B_1$  inhomogeneity, which is con-

sidered especially important. The RF pulse simulation helped the understanding of signal behavior using non-ideal slice-selective RF pulses, and also improved the fitting algorithm. Reproducible results measured in a group of volunteers agreed well with literature values. The comparison with reference methods showed good correspondence of the obtained values. However, a rapid method is clearly essential for quantification, because the long scan time of all reference methods combined unavoidably leads to misregistration and thus inaccurate results, especially for PD.

Care should be taken in the interpretation of the absolute MR parameters. In our approach, using only a low number of relaxation data points, we assume a monoexponential decay for the relaxation times. For many tissues,  $T_1$  and  $T_2$  relaxation might be multiexponential (10,11), which reflects an underlying partition of the water in various microscopic environments, and is often considered for data analysis using stretched exponentials. Furthermore, note that the brain anatomies are far more complex and differentiated than what appears in Table 1. The SD of the values within a single volunteer is larger than the SD within the whole group, suggesting that part of the variance in the absolute values is due to intrinsic tissue inhomogeneity rather than to noise. For clinical use, however, it is important to find a consistent change of tissue parameters as compared to normal values. From Table 1, it is clear that healthy tissue has a narrow range of values that can be taken as a reference value and to distinguish pathology.

An example of clinical absolute quantification is shown on a patient afflicted by MS. The lesions inside the WM clearly show up as a simultaneous increase of  $T_1$ ,  $T_2$ , and PD. Using conventional imaging, only the most pronounced affected areas can be distinguished, and various ways of relating area size to the clinical symptoms of the

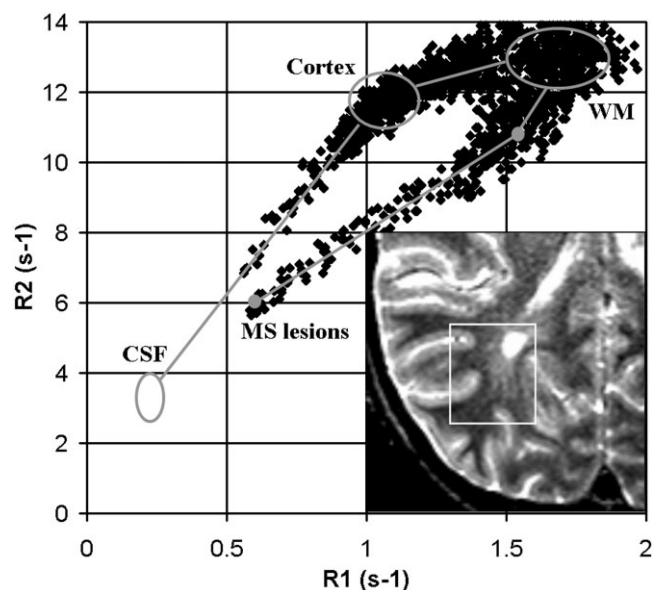


FIG. 8. Similar scatter plot as in Fig 7, applied on a patient with MS. The apparent two phases of MS lesion development are indicated by the two gray lines separated by dots.



disease have been proposed (e.g., Refs. 23–25). Based on contrast images alone, with significant variation between MR scanners related to scanner parameters and particular software versions, it is very difficult to reliably automatically segment the plaques (26,27). Using absolute quantification, however, the scanner dependency is in principle removed and the deviation from normal WM and the absolute progress of the lesions can be accurately visualized, as shown in Figs. 7 and 8.

It is important to note that the signal of flowing blood is suppressed in the QRAPMASTER sequence. This might explain the nearly equal relaxation values of the MS patient before and after Gd injection, since the blood component of the effective relaxation per voxel is not visible. An actual blood-brain-barrier leakage, however, would show up, since the infiltrated brain tissue is static. Using the relaxation parameters, the partial volume of the tissue can be calculated and a more accurate measure for the stage and total volume of MS lesions could potentially be retrieved with sufficient accuracy for clinical diagnosis. This is a promising result and invites further investigation. Other clinical examples of quantification with important partial volume effects are the estimation of excess water content in case of edema or the extent of neurosarcoidosis.

A future widespread clinical use of absolute quantification of the MR parameters could be facilitated by the application of synthetic MRI. Figure 6 shows that the synthetic contrast images, based on the absolute parameter maps of Fig. 5, reflect tissue contrast very similar to that observed in conventional contrast images. An important difference between conventional and synthetic contrast images is that the latter are based on absolute values. Not only do the images have perfect registration, but all scanner dependencies, such as  $T_R$ ,  $T_E$ , or  $B_1$  inhomogeneity, are in fact merely artificially added parameters for familiarity. Since synthetic MRI allows the computation of an infinite number of different contrast-weighted images, it could be a very useful technique for screening purposes with any relevant combination of the scanner settings  $T_E$ ,  $T_R$ ,  $\alpha$ , and  $T_{IR}$  when the optimal set of contrast parameter settings is unknown a priori. A radiologist could have the absolute parameter maps next to the apparently normal contrast images based on the same quantification scan. Potentially, this combination might replace the acquisition of a whole series of conventional images and perhaps save valuable scanner time.

## CONCLUSIONS

The presented QRAPMASTER method describes rapid quantification of  $T_1$  and  $T_2$  relaxation, PD, and  $B_1$  field, covering the brain at high resolution in a scan time of only 5 min. Such an absolute measurement would support diagnosis with quantitative values for the progress of diseases. Validation was done on a group of volunteers and a clinical example of the technique application on a patient with multiple sclerosis is shown. Synthetic contrast images were generated from the same quantification data set as a visual aid for the clinical radiologist to verify the results without the need to use a plethora of different

acquisition series that consume valuable scanning time. We expect that rapid quantification and subsequent image synthesis will be an important clinical tool in the near future.

## ACKNOWLEDGMENTS

Synthetic MR Technologies AB (<http://www.synthetic-mr.se>) provided support on the synthesis of MR contrast images.

## REFERENCES

1. Tofts P. Quantitative MRI of the brain. New York: Wiley, 2003.
2. Warntjes JBM, Dahlqvist O, Lundberg P. A novel method for rapid, simultaneous  $T_1$ ,  $T_2^*$  and proton density quantification. *Magn Reson Med* 2007;57:528–537.
3. Neeb H, Zilles K, Shah NJ. A new method for fast quantitative mapping of absolute water content in vivo. *Neuroimage* 2006;31:1156–1168.
4. Deoni SCL, Rutt BK, Peters TM. High-resolution  $T_1$  and  $T_2$  mapping of the brain in a clinically acceptable time with DESPOT1 and DESPOT2. *Magn Reson Med* 2005;53:237–241.
5. Deoni SCL. High-resolution  $T_1$  mapping of the brain at 3T with driven equilibrium single pulse observation of  $T_1$  with high-speed incorporation of RF field inhomogeneities (DESPOT1-HIFI). *J Magn Reson Imaging* 2007;26:1106–1111.
6. Deichmann R. Fast high-resolution  $T_1$  mapping of the human brain. *Magn Reson Med* 2005;54:20–27.
7. Zhu DC, Penn RD. Full brain  $T_1$  mapping through inversion-recovery fast spin echo imaging with time-efficient slice ordering. *Magn Reson Med* 2005;54:725–731.
8. Ordidge RJ, Gibbs P, Chapman B, Stehling MK, Mansfield P. High-speed multi-slice  $T_1$  mapping using inversion recovery echo planar imaging. *Magn Reson Med* 1990;16:238–245.
9. Clare S, Jezzard P. Rapid  $T_1$  mapping using multislice echo planar imaging. *Magn Reson Med* 2001;45:630–634.
10. Whittall KP, MacKay AL, Douglas AG, Graeb DA, Nugent RA, Li DKB, Paty DW. In vivo measurements of  $T_2$  distributions and water contents in normal human brain. *Magn Reson Med* 1997;37:34–43.
11. MacKay A, Laule C, Vavasour I, Bjarnason T, Kolind S, Mädlar B. Insights into brain microstructure from the  $T_2$  distribution. *Magn Reson Imaging* 2006;24:515–525.
12. Oh J, Cha S, Aiken AH, Han ET, Crane JC, Stainsby JA, Wright GA, Dillon WP, Nelson SJ. Quantitative apparent diffusion coefficients and  $T_2$  relaxation times in characterizing contrast enhancing brain tumors and regions of peritumoral edema. *J Magn Reson Imaging* 2005;21:701–717.
13. McKenzie CA, Chen Z, Drost DJ, Prato FS. Fast acquisition of quantitative  $T_2$  maps. *Magn Reson Med* 1999;41:208–212.
14. Ernst T, Kreis R, Ross BD. Absolute quantitation of water and metabolites in the human brain. 1: Compartments and water. *J Magn Res Ser B* 1993;102:1–8.
15. Riederer SJ, Lee JN, Farzaneh F, Wang HZ, Wright RC. Magnetic resonance image synthesis: clinical implementation. *Acta Radiol Suppl* 1986;369:466–468.
16. Bobman SA, Riederer SJ, Lee JN, Suddarth SA, Wang BP, Drayer BP, MacFall JR. Cerebral magnetic resonance image synthesis. *AJR Am J Neuroradiol* 1985;6:265–269.
17. Redpath TW, Smith FW, Hutchison JM. Magnetic resonance image synthesis from an interleaved saturation recovery/inversion recovery sequence. *Br J Radiol* 1988;61:619–624.
18. Zhu XP, Hutchinson CE, Hawnaur JM, Coates TF, Taylor CJ, Isherwood I. Magnetic resonance image synthesis using a flexible model. *Br J Radiol* 1994;67:976–982.
19. Gulani V, Schmitt P, Griswold MA, Webb AG, Jakob PM. Towards a single-sequence neurologic magnetic resonance imaging examination: multiple-contrast images from an IR TrueFISP experiment. *Invest Radiol* 2004;39:767–774.
20. Hacklander T, Mertens H. Virtual MRI: a PC-based simulation of a clinical MR scanner. *Acad Radiol* 2005;12:85–96.

21. Haacke EM. Magnetic resonance imaging, physical principles and sequence design. New York: Wiley, 1999.
22. Kellman P, Arai AE, McVeigh ER, Aletras AH. Phase-sensitive inversion recovery for detecting myocardial infarction using gadolinium-delayed hyperenhancement. *Magn Reson Imaging* 2002;47:372–282.
23. Bakshi R, Hutton GJ, Miller JR, Radue EW. The use of magnetic resonance imaging in the diagnosis and long-term management of multiple sclerosis. *Neurology* 2004;63:S3–S11.
24. Fazekas F, Soelberg-Sorensen P, Comi G, Filippi M. MRI to monitor treatment efficacy in multiple sclerosis. *J Neuroimaging* 2007;17:50S–55S.
25. Neema M, Stankiewicz J, Arora A, Dandamudi VS, Batt CE, Guss ZD, Al-Sabbagh A, Bakshi R. T1- and T2-based MRI measures of diffuse gray matter and white matter damage in patients with multiple sclerosis. *J Neuroimaging* 2007;17:16S–21S.
26. Datta S, Sajja BR, He R, Gupta RK, Wolinsky JS, Narayana PA. Segmentation of gadolinium-enhanced lesions on MRI in multiple sclerosis. *J Magn Reson Imaging* 2007;25:932–937.
27. Achiron A, Gicquel S, Miron S, Faibel M. Brain MRI lesion load quantification in multiple sclerosis: a comparison between automated multispectral and semi-automated thresholding computer-assisted techniques. *Magn Reson Imaging* 2002;20:713–720.